



**HAL**  
open science

## Deep structure of the Baikal rift zone revealed by joint inversion of gravity and seismology

C Tiberi, M Diament, Jacques Déverchère, C Petit-Mariani, V Mikhailov, S Tikhotsky, U Achauer

### ► To cite this version:

C Tiberi, M Diament, Jacques Déverchère, C Petit-Mariani, V Mikhailov, et al.. Deep structure of the Baikal rift zone revealed by joint inversion of gravity and seismology. *Journal of Geophysical Research: Solid Earth*, 2003, 108 (B3), pp.2109. 10.1029/2002JB001880 . insu-01356068

**HAL Id: insu-01356068**

**<https://insu.hal.science/insu-01356068>**

Submitted on 24 Aug 2016

**HAL** is a multi-disciplinary open access archive for the deposit and dissemination of scientific research documents, whether they are published or not. The documents may come from teaching and research institutions in France or abroad, or from public or private research centers.

L'archive ouverte pluridisciplinaire **HAL**, est destinée au dépôt et à la diffusion de documents scientifiques de niveau recherche, publiés ou non, émanant des établissements d'enseignement et de recherche français ou étrangers, des laboratoires publics ou privés.

## Deep structure of the Baikal rift zone revealed by joint inversion of gravity and seismology

C. Tiberi,<sup>1,2</sup> M. Diament,<sup>3</sup> J. Déverchère,<sup>4</sup> C. Petit-Mariani,<sup>5</sup> V. Mikhailov,<sup>6</sup> S. Tikhotsky,<sup>6</sup> and U. Achauer<sup>7</sup>

Received 19 March 2002; revised 27 September 2002; accepted 18 November 2002; published 7 March 2003.

[1] The question of plate boundary forces and deep versus shallow asthenospheric uplift has long been debated in intracontinental rift areas, particularly in the Baikal rift zone, Asia, which is colder than other continental rifts. As previous gravity and teleseismic studies support the dominance of opposing mechanisms in the Baikal rift, we reconsidered both data sets and jointly inverted them. This more effective approach brings insight into location of the perturbing bodies related to the extension in this region. Our new joint inversion method allows for inverting the velocity-density relationship with independent model parametrization. We obtain velocity and density models that consistently show (1) crustal heterogeneities that coincide with the main tectonic features at the surface, (2) a faster and denser cratonic mantle NW of Lake Baikal that we relate to the thermal contrast between old and depleted Archean (Siberian platform) and Paleozoic orogenic belt (Sayan-Baikal belt), (3) three-dimensional topographic variations of the crust-mantle boundary with well-located upwarps, and (4) the lithosphere-asthenosphere boundary uplift up to 70 km depth with a NW dip. Our resulting velocity and density models support the idea of a combined influence of lithospheric extension and inherited lithospheric heterogeneities for the origin of the Baikal rift zone.

*INDEX TERMS:* 1234 Geodesy and Gravity: Regional and global gravity anomalies and Earth structure; 7218 Seismology: Lithosphere and upper mantle; 8122 Tectonophysics: Dynamics, gravity and tectonics; 8180 Tectonophysics: Evolution of the Earth: Tomography; *KEYWORDS:* joint inversion, gravity, seismology, intracontinental rift, lithospheric structures, Baikal rift zone

**Citation:** Tiberi, C., M. Diament, J. Déverchère, C. Petit-Mariani, V. Mikhailov, S. Tikhotsky, and U. Achauer, Deep structure of the Baikal rift zone revealed by joint inversion of gravity and seismology, *J. Geophys. Res.*, 108(B3), 2133, doi:10.1029/2002JB001880, 2003.

### 1. Introduction

[2] Active continental rifts constitute unique laboratories to determine the role of the different driving forces involved in the early stages of continental break-up. The development of intracontinental rift is governed by a number of processes, including asthenospheric upwellings or plumes, and/or far field stresses due to plate boundary or sublithospheric drag (see *Ruppel* [1995] for an overview). The inherited

lithospheric rheology and structure are also known to strongly influence the development of rift systems [e.g., *Petit et al.*, 1996; *Tommasi and Vauchez*, 2001]. However, the relative importance of each process is still not clearly determined in many continental rift zones mainly because these factors may overlap in space and/or time [e.g., *Ruppel*, 1995; *Huismans et al.*, 2001]. Particularly, the Baikal rift system has been the focus of a large debate about driving forces.

[3] The Baikal rift is the largest Eurasian intracontinental rift zone situated at the southern border of the Siberian craton far from any plate boundary (Figure 1). The far field stresses that could drive the Baikal rift are believed to be influenced by the Indo-Asian collision [*Molnar and Tapponnier*, 1975], by the subduction of the Pacific plate [*Nataf et al.*, 1981] and by the lithospheric structure inherited from previous orogenic fabrics [*Petit et al.*, 1996; *Lesne et al.*, 2000]. Alternatively, *Zorin* [1981] and *Gao et al.* [1994] advocate an active asthenospheric upwelling to explain the rifting process in Baikal, even arguing that its apex reaches the Moho. However, evidences for an active asthenospheric upwelling from teleseismic and gravity data [*Zorin et al.*, 1989; *Gao et al.*, 1994] have been contradicted by other recent gravity and geochemical studies [*Petit et al.*, 1998;

<sup>1</sup>Department of Geology, Royal Holloway University of London, Egham, UK.

<sup>2</sup>Now at Laboratoire de Tectonique UMR 7072, Université Paris 6, Paris, France.

<sup>3</sup>Laboratoire de Gravimétrie et Géodynamique, Département de Géophysique Spatiale et Planétaire UMR 7096, Institut de Physique du Globe, Paris, France.

<sup>4</sup>Institut Universitaire Européen de la Mer, Domaines Océaniques UMR 6538, Université de Bretagne Occidentale, Brest-Iroise, France.

<sup>5</sup>Laboratoire de Tectonique UMR 7072, Université Paris 6, Paris, France.

<sup>6</sup>Institute of Physics of the Earth RAS, Moscow, Russia.

<sup>7</sup>Manteau et Sismologie Large Bande, Ecole et Observatoire des Sciences de la Terre, Strasbourg, France.

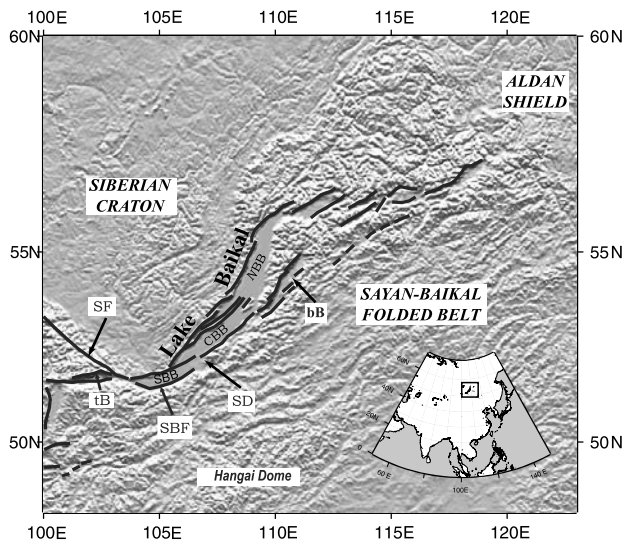


**Figure 1.** Topography and map location for the main faults and structural units in the vicinity of the Baikal rift zone. SD = Selenga delta, bB = Barguzin basin, SBF = South Baikal fault, SF = Sayan fault, SBB = South Baikal basin, CBB = Center Baikal basin, NBB = North Baikal basin, tB = Tunka basin.

Garner *et al.*, 2001; Ionov, 2002]. Such an upwelling seems also contradictory to the high effective elastic thickness found in this area (about 50 km, e.g., Diament and Kogan [1990]) and the regional low heat flow [Lysack, 1992].

[4] We present a joint inversion of gravity and teleseismic data to clarify this problem and to resolve the ambiguity coming from separate gravity and seismological studies [Jordan and Achauer, 1999]. We combine the gravity data in the Baikal rift zone with the delay time data from two experiments carried out in the 90s, in the framework of an American-Russian collaborative project [Gao *et al.*, 1994, 1997]. The inversion scheme is based on the theory proposed by Zeyen and Achauer [1997], improved by three-dimensional (3-D) raytracing and independent density and velocity model parametrization. Both data sets were simultaneously interpreted in terms of density and velocity perturbations in the crust and upper mantle. It thus offers insight into the rift structure beneath Lake Baikal and its surroundings down to about 200 km. We compare the distribution of density and velocity in the upper part of the models with the main geological features of the region. We then interpret the upper mantle part of our models in term of cooling. Finally, we discuss evidence against the idea of asthenospheric upwelling rising up to the base of the crust below the rift.

## 2. Tectonic Setting and Deep Structure

[5] The Baikal rift zone has developed along the suture of the Archean Siberian craton and the Paleozoic Sayan-Baikal orogenic belt (Figure 1). The junction of these Archean and Paleo-Mesozoic terranes provides an inherited lithospheric fabric that has influenced the location and the evolution of the Baikal rift, as proposed in most continental rifts [e.g., Nicolas *et al.*, 1994; Vauchez *et al.*, 1997, 1998]. The seismically active 2000 km en echelon system of rift depressions

follows this S-shape Paleozoic suture in its central part, and is dominated by extensional tectonics with a strike-slip component [Déverchère *et al.*, 1993]. The seismic pattern is in good agreement with recent GPS data that indicate a crustal extension of  $4.5 \text{ mm yr}^{-1}$  in a WNW-ESE direction [Calais *et al.*, 1998]. It seems that extensional processes have reached a fast rifting stage for the last 3 My [Logatchev and Zorin, 1987; Hutchinson *et al.*, 1992], although this was recently questioned by seismic investigations [ten Brink and Taylor, 2002].

[6] Previous studies in the Baikal rift zone have led to contrasting interpretations regarding its deep structure and the driving mechanisms. In their teleseismic study, Gao *et al.* [1994] proceed to a downward projection, assuming that the delay times arise from the geometry of the lithosphere-asthenosphere boundary. They conclude that the top of the asthenosphere has an asymmetrical shape with an apex that reaches the Moho level (34 km) in the vicinity of the lake. That is to say that in this area the lithosphere comprises only crust. Some previous gravity interpretations also proposed the existence of an asthenospheric upwelling [Logatchev *et al.*, 1983; Zorin *et al.*, 1989]. A deep crustal seismic study reports evidence against a low velocity zone ( $7.8 \text{ km s}^{-1}$ ) beneath the Moho close to the rift axis [ten Brink and Taylor, 2002]. The same study reports an average Moho depth of 42 km in the Central Basin, and mantle velocity of  $8.0 \text{ km s}^{-1}$ . This is in good agreement with the regional low heat flow observed in this region ( $40\text{--}60 \text{ mW m}^{-2}$  after Lysack [1992]) and the lack of volcanism. Mantle xenolith analysis [Ionov *et al.*, 1995; Ionov, 2002] as well as gravity modeling [Petit *et al.*, 1997] and models of the mechanical behavior of the lithosphere [Ruppel *et al.*, 1993; Burov *et al.*, 1994] also show that the lithosphere beneath the lake is not significantly thinned. Dense seismicity distribution down to 35 km depth in this region also indicates a cold and strong lithosphere [Déverchère *et al.*, 2001]. A recent surface wave tomographic study also shows no large deep root below the Baikal rift zone [Priestley and Debayle, 2001]. Unfortunately, global tomographic studies carried out in the vicinity of the region do not manage to provide a detailed lithospheric model of the rift zone [Koulakov, 1998; Villaseñor *et al.*, 2001].

[7] The differences in interpreting deep structure mainly come from considering separately independent sets of data. Solution of the inverse problem from separate methods is very often nonunique. For example, idea of an asthenospheric upwelling contradicts the deep crustal seismicity, low heat flow, and lack of volcanism. We attempt here to reconcile the gravity and seismological data by jointly inverting them. When constraining the interpretational model we tried to take into account other existing geophysical and geological data.

## 3. Data Processing

[8] The first independent data set we used for the joint inversion is made by the 1792 teleseismic P wave delay times from Gao *et al.* [1994, 1997], registered at 53 stations from 155 earthquakes. The residuals were calculated using IASP reference Earth model. The second data set is the complete Bouguer anomaly for the Baikal region averaged on a  $15' \times 10'$  grid from TsNIIGAiK database (Moscow, Russia) by courtesy of G. Demianov (Figure 2). The com-

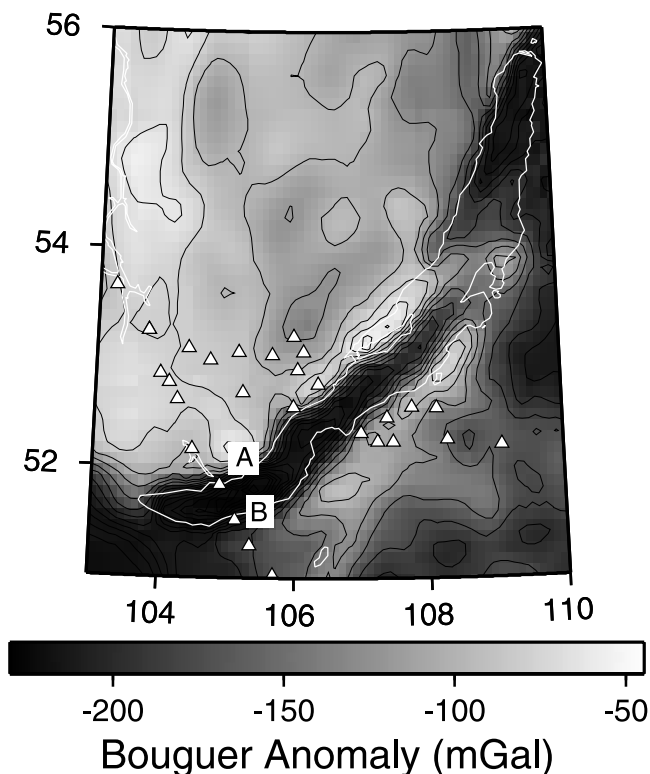


**Figure 2.** Complete Bouguer anomaly for the Baikal region. The white triangles are the seismological station locations [from Gao *et al.*, 1994; Gao *et al.*, 1997].

plete Bouguer anomaly was computed using an average density of  $2670 \text{ kg m}^{-3}$  for topographic loads.

[9] The coherent behavior of these two data sets (Figure 3) justifies the use of a linear correlation coefficient (hereafter referred to as B-factor) between density and velocity which is constant within specified depth intervals of the crust and mantle [Abers, 1994].

[10] The two lowest Bouguer values (Figure 3) correspond to the two southernmost stations near the edges of Lake Baikal (stations A and B, Figure 2), where sediment effects can be of great significance [Hutchinson *et al.*, 1992]. The sediments are located in the upper 10 kilometers of the crust, where we expect very poor teleseismic ray crossing. Thus, the 7 kilometers of sedimentary strata should have more effect on the gravity than on the mean delay-time. We therefore have corrected the gravity signal for the sedimentary and water infills inside the lake using bathymetry and seismic cross sections [Hutchinson *et al.*, 1992; ten Brink and Taylor, 2002]. To take into account the compaction, the density assumed for the sedimentary infill increases with depth. We fixed a value of  $2200 \text{ kg m}^{-3}$  from the surface down to two kilometers depth,  $2400 \text{ kg m}^{-3}$  from 2 to 4 km depth, and  $2600 \text{ kg m}^{-3}$  from 5 to 6 km depth. This correction leads to a maximum value of  $-140 \text{ mGal}$  for the Baikal region. This sediment correction improves the linear relationship between the two sets of data (Figure 3, black circles).

#### 4. Joint Inversion of Gravity and Delay Times

[11] The term “cooperative inversion” of geophysical data, and particularly between seismic and gravity data,

was defined by Lines *et al.* [1988]. They discerned between joint and sequential inversion. The sequential method treats the two data set separately, whereas the joint one simultaneously places them into one data vector. Earlier cooperative inversions of Bouguer and delay time data, either sequential [Vernant *et al.*, 2002] or joint [Lees and VanDecar, 1991] consider a constant linear relationship between density and velocity [e.g., Birch, 1961]. The approach we used here is based on the suggestion of Zeyen and Achauer [1997] and Jordan and Achauer [1999], to treat the B-factor linking velocity and density ( $\Delta V_p = \mathbf{B}\Delta\rho$ ) as a parameter allowed to vary around a given value. Especially, it can take different values with depth, and thus can better depict the correlation between velocity and density. This improvement leads in turn to a nonlinear (iterative) inversion scheme. Our method is based on the Bayesian approach with the possibility of including any a priori information. It differs from the initial approach of Zeyen and Achauer [1997] in that it uses a 3-D raytracing [Steck and Prothero, 1991] and an independent parametrization for density (block gridding) and velocity (node gridding) models.

#### 4.1. Model Parametrization

[12] The joint inversion requires for the 3-D velocity and density models to have the same layer boundaries in depth, so that a B-factor linking these parameters can be defined for each layer. However, in this method the horizontal limits can differ, allowing the user to parametrize the volume more freely. Each layer is then subdivided into density blocks, and velocity nodes (Figure 4). A density contrast is assigned to each block, and each node corresponds to one velocity value. The interpolation between each velocity node of this 3-D grid is proceeded with the pseudo linear gradient method [Thurber, 1983]. The calculation of the gravity anomaly corresponding to the 3-D model is simply performed by adding the vertical attraction due to the collection of rectangular prisms in each layer [e.g., Blakely, 1995; Li and Chouteau, 1998].

[13] This parametrization permits to densify the grid where the data coverage or the station location allows for

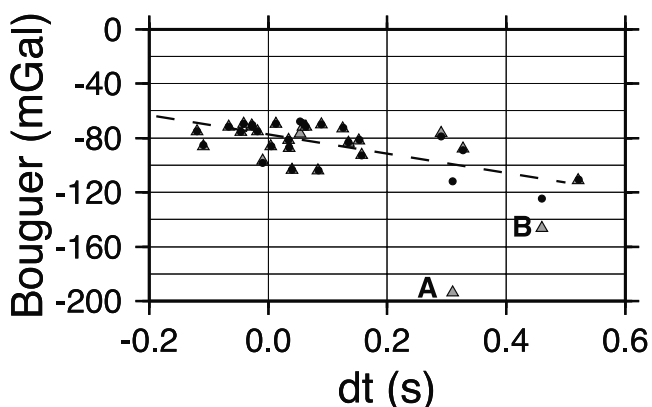


**Figure 3.** Complete Bouguer anomaly versus mean P wave delay time at each station. Grey triangles represent the stations before water and sediments correction, black circles represent the stations after correction. The dashed line is the best regression line for the corrected values. The letters A and B refer to the locations of two stations in Figure 2.

a better accuracy. The average seismological station spacing and data gridding determine the smallest block and node spacing. We are working in a zero mean assumption in this method, so that for each layer, the average density and velocity values are subtracted from the initial ones.

#### 4.2. Inversion Formulation

[14] The method tries to find the best fitting model in the least squares sense that simultaneously explains the gravity and the delay times data. In other words, we try to minimize the difference between observed ( $\vec{d}$ ) and calculated ( $\vec{c}$ ) data. In order to take into account the difference in data accuracy, a square diagonal covariance matrix  $C_d$  is defined, and the first expression to be minimized is then:

$$(\vec{d} - \vec{c})^t \cdot C_d^{-1} \cdot (\vec{d} - \vec{c}) \quad (1)$$

where symbol  $^t$  denotes here and hereafter transform matrix. As most of geophysical inverse problems, the joint inversion is ill-posed. A part of the data can be redundant, and some parameters will not be inverted (typically velocity nodes not crossed by teleseismic rays). To regularize this problem, *Zeyen and Achauer* [1997] proposed three different methods that lead to additional expressions to be minimized. The first one is to include a priori informations in the problem. This kind of informations can be obtained in two ways. Known velocities or densities in some areas, resulting from previous geophysical studies for instance, can be included in a starting model ( $\vec{p}_0$ ). We can also introduce a parameter covariance matrix  $C_p$  that will allow more or less changes in the parameter value through the iterations. This a priori information can be expressed as the following equation to be minimized:

$$(\vec{p} - \vec{p}_0)^t \cdot C_p^{-1} \cdot (\vec{p} - \vec{p}_0) \quad (2)$$

Where  $\vec{p}$  refers to the parameter vector (i.e., velocity and density contrasts and  $B$ -values), and  $\vec{p}_0$  to the previous iteration values of the parameter vector. The relationship between velocity and density is a second way to regularize the ill-posed problem. In this method, the  $B$ -factor is an unknown parameter and is inverted independently for each layer. This allows to take into account its temperature dependence with depth. Here again, a covariance matrix  $C_b$  is defined to control the amount of  $B$ -factor variation. This square matrix is diagonal, and the smaller its elements, the stricter the linear relation between velocity and density. This leads to the following term to be minimized:

$$(\vec{\Delta V} - \vec{B}\vec{\Delta\rho})^t \cdot C_b^{-1} \cdot (\vec{\Delta V} - \vec{B}\vec{\Delta\rho}) \quad (3)$$

where  $\vec{\Delta V}$ ,  $\vec{\Delta\rho}$  and  $\vec{B}$  are the vectors of velocity contrast, density contrast and  $B$ -values. In our inversion, all the density blocks are inverted. Thus, in order not to put too much signal in gravity cells without velocity information, we introduce a smoothing constraint. For that purpose, we use the first derivatives of the parameters  $\frac{\Delta p}{\Delta R}$ . Here,  $\Delta p$  refers to the difference of parameter between adjacent blocks, and  $\Delta R$  corresponds to the distance between these blocks. A covariance matrix  $C_s$  is also introduced to control

the importance of this condition relative to the other ones. The expression to be minimized is then:

$$\left(\frac{\vec{\Delta p}}{\Delta R}\right)^t \cdot C_s^{-1} \cdot \left(\frac{\vec{\Delta p}}{\Delta R}\right) \quad (4)$$

[15] We then derive the sum of all the previous equations (1) to (4) to find the following expression to solve:

$$\vec{p} = \vec{p}_0 + (A^t C_d^{-1} A + C_p^{-1} - C_b^{-1} D_b - C_s^{-1} D_s)^{-1} \cdot (A^t C_d^{-1} (\vec{d} - \vec{c}) + C_b^{-1} \vec{b} + C_s^{-1} \vec{s}) \quad (5)$$

where  $A$  is the matrix of partial derivatives of the calculated data  $\vec{c}$  relative to the parameters  $\vec{p}$ .  $D_b$  and  $\vec{b}$  are matrix and vector related to the velocity-density relationship (equation (3)), respectively.  $D_b$  is a symmetric matrix with different blocks corresponding to cross-products between velocity, density and  $B$ -value. The vector  $\vec{b}$  basically corresponds to the  $\vec{\Delta V} - \vec{B}\vec{\Delta\rho}$  expression of equation (3). Their detailed compositions are given by *Zeyen and Achauer* [1997].  $D_s$  and  $\vec{s}$  are the matrix and vector corresponding to the roughness control of the model (equation (4)), respectively. The elements of  $D_s$  are composed by the sum of the distances between adjacent blocks, and the vector  $\vec{s}$  contains the difference between parameters of adjacent blocks weighted by their distance.

[16] As shown in equation (5), we obtain an iterative procedure to calculate the new parameter vector  $\vec{p}$ . The flowchart in Figure 4 presents the different steps of the calculation.

[17] First, we calculate the delay times and the gravity anomaly corresponding to the input model ( $\vec{p}_0$ ). Then the difference between measured and calculated data is computed. If this difference is smaller than a given threshold (epsilon) set by the operator, then the process stops and outputs the final density and velocity models. If not, the difference between observed and calculated data is used to compute a new set of parameters (according to equation (5)). If the number of iterations is reached then the process outputs the resulting density and velocity models with a  $B$ -value for each layer of the model. If not, it goes for a new round through the whole process and takes the output models and  $B$ -values to forward calculate the delay times and gravity anomaly.

[18] At the end of iterations, the resolution matrix is calculated following the expression:

$$R = \left(A^t C_d^{-1} A + C_p^{-1} - C_b^{-1} D_b - C_s^{-1} D_s\right)^{-1} A^t C_d^{-1} A \quad (6)$$

and it allows to link the “true” model of the Earth to the solution we got. The density and velocity parts of the resolution matrix are separated.

#### 4.3. Main Parameters Used in the Baikal Rift Zone

[19] Velocity nodes are constrained and inverted if more than 5 teleseismic rays pass in their vicinity. Initial velocity and density models were constrained by the results of recent OBS seismic studies in the region [*ten Brink and Taylor*,

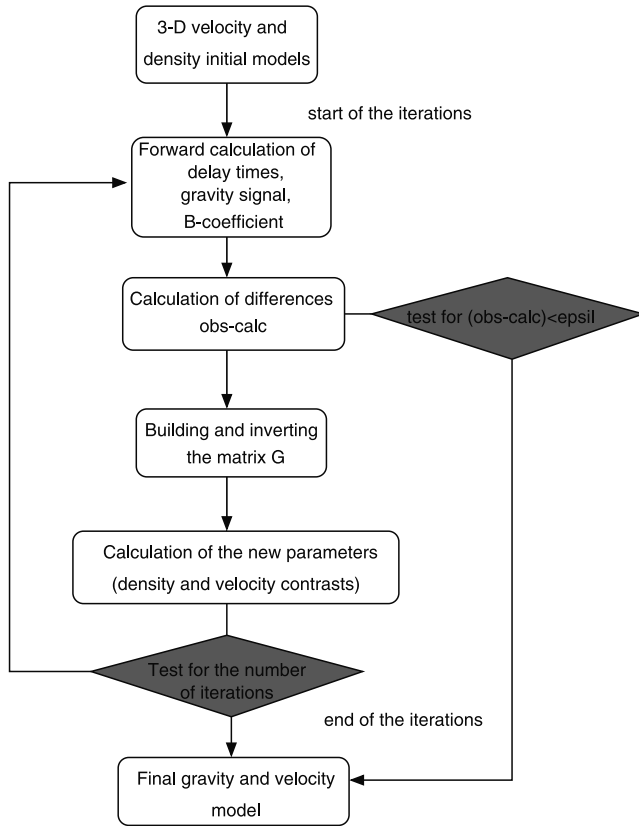


**Figure 4.** Flowchart of the joint inversion procedure. The matrix  $G$  refers to the one in brackets in equation (5), and  $\epsilon$  is a threshold set by the user to stop the iterations (see text for detailed explanation).

2002], local travel time analysis [Petit and Déverchère, 1995; Petit et al., 1998] and commonly used density values for the crust and mantle (Table 1). The density block size varies from 25 to 100 km, widening grid with depth. The velocity nodes were laterally spaced by 50 to 300 km. As the  $B$ -initial values are commonly taken between 2 and 5  $\text{km s}^{-1} \text{g}^{-1} \text{cm}^3$  [e.g., Abers, 1994; Tiberi et al., 2001], we chose here an average value around 3  $\text{km s}^{-1} \text{g}^{-1} \text{cm}^3$  (Table 1), with a standard variation of 0.1  $\text{km s}^{-1} \text{g}^{-1} \text{cm}^3$ . The choice of this parameter will be discussed later in the next section. The data standard deviations were set to 5 mGal and 0.1 s for the Bouguer gravity and the delay times, respectively. We chose a constant standard error of 0.3  $\text{km s}^{-1}$  for the velocity and a standard error of 300  $\text{kg m}^{-3}$  for the density. The standard deviation remains constant for the parameters in order to take into account the lack of a priori information in depth for the region. We preferred to favor a homogeneous starting model in this case. The density and velocity grids are wider than the area of gravity data coverage to get rid of possible boundary effects. As the nodes and blocks outside the data area are poorly constrained, we do not represent them on the resulting models.

## 5. Resulting Velocity and Density Models

[20] The resulting velocity and density models obtained after jointly inverting the data sets are presented in the first part of this section. In a second part, we discuss which

perturbations are the most trustable in our final model in light of several tests reported in detail in the annexes.

### 5.1. Main Density and Velocity Perturbations

[21] The resulting density and velocity models are shown on Figure 5. Two cross sections along the two main teleseismic profiles are also reported in Figure 6. It is worth noting here that the density contrasts and velocity variations were calculated in each layer relative to a reference value, with zero average. So one cannot directly compare the variations between two different layers. That is the reason why the cross sections in Figure 6 are not smoothed over the vertical axis. Hence, velocity and density variations mainly reflect topography of density/velocity interfaces or perturbing bodies within each layer. The models presented on Figures 5 and 6 result from three iterations. The overall decrease of the root mean square (rms) is 70.4% and 49.2% for the gravity and delay time data, respectively (Figure 7). Standard deviations of the calculated data are 22.9 mGal for gravity and 0.2 s for delay times. They are fairly close to those of the initial data (24.6 mGal and 0.3 s, respectively). The evolution of  $B$ -factor during the iterations is reported in Figure 8, and the correlation between velocity and density contrasts is more than 91% for the different layers (Figure 9).

[22] The diagonal elements of the resolution matrix are represented in Figures 10 and 11 for both the density and velocity models. The resolution terms are fairly high in the superficial layers for the density (max. at 0.99 for the first layer) and decrease rapidly in the deeper layers to reach a maximum of 0.11 in the deepest one. In our inversion, gravity anomalies are more suited to reflect the superficial items than the deep ones. The calculated gravity from the density model shows only small short wavelength differences with the observed anomaly, reflecting a good agreement between our model and data (Figure 12). The short wavelength residuals are directly related to our coarse grid size dictated by seismic coverage. The resolution of the velocity increases with depth from the edges to the center of the model. The deeper, the better the ray cross-fired, and the better the resolution. Nevertheless, even the first layers present good resolution thanks to the gravity constraint. Figure 11 shows a lack of resolution for the uppermost layers in the region between the two main profiles, near the Selenga delta (SG in Figure 1). We performed synthetic tests that show that a  $80 \times 60 \text{ km}$  perturbing body located in layers 2 and 3 (+10% velocity anomaly corresponding to +230 and +270  $\text{kg m}^{-3}$  density contrast) can be completely retrieved after inversion in density model when located in the middle of the two profiles (estimated density contrast was equal to +300  $\text{kg m}^{-3}$ ). The velocity model only partially retrieves the anomaly, with a +1.5% velocity

**Table 1.** Initial Velocity and Density Models and Starting Parameters Used for the Joint Inversion

Layer	Depth Range, km	$V_p$ , $\text{km s}^{-1}$	$\rho$ , $\text{kg m}^{-3}$	Initial $B$ , $\text{km s}^{-1} \text{g}^{-1} \text{cm}^3$
1	0–20	6.00	2670	3.00
2	20–40	7.00	2900	3.00
3	40–60	8.00	3200	3.30
4	60–80	8.05	3250	3.30
5	80–140	8.10	3300	3.30
6	140–200	8.20	3350	3.30

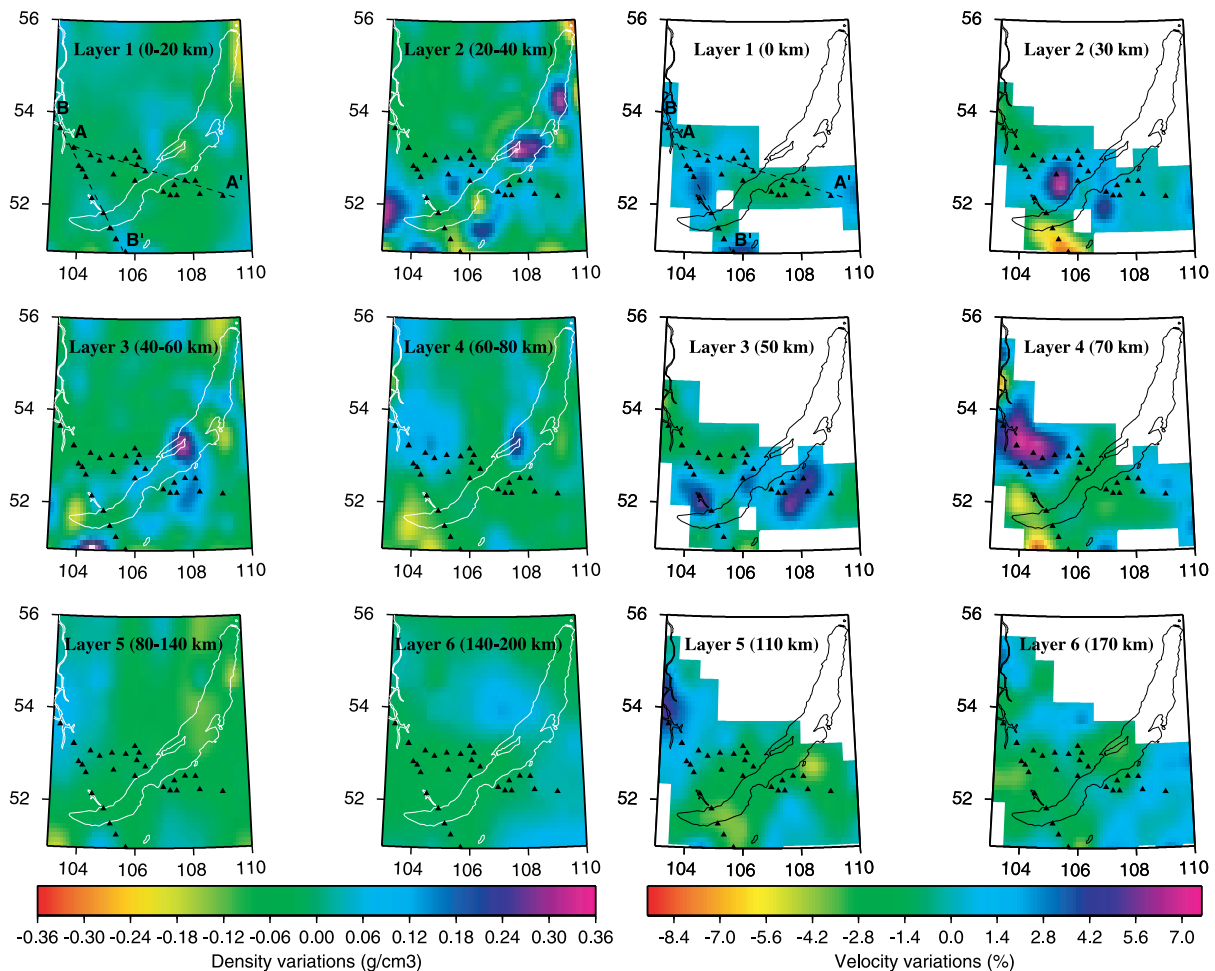


**Figure 5.** Density (left) and velocity (right) models of the different layers obtained in result of the joint inversion.

perturbation in the vicinity of the stations that are close to the perturbing body. Thus the addition of gravity information compensates here the poor ray-crossing of seismic data, and we expect to obtain more information from the density model in this area for the upper layers.

[23] Our results show that the structure of heterogeneities is largely three-dimensional. The resulting contrasts are in the range  $-440 + 620 \text{ kg m}^{-3}$  for the density and  $-14.88\% + 10.59\%$  for the velocity perturbations. As a whole, there is a very good consistency between density and velocity models for every layer (Figures 5 and 9). The two upper layers present less consistency because of less resolved velocity nodes (Figure 11). The shortest wavelengths are observed in the upper layers, whereas the three deepest ones are mainly dominated by contrasts at long wavelengths. This is partly coming from the different size of density blocks. The maximum density and velocity contrasts are located in layers 2 to 4, with sharp lateral gradients between the perturbations. The first layer contains a very small density contrast. As a whole, within layer 3 the velocity and density are well correlated. Two high density features appear in regions without velocity resolution (western end and central part of Lake Baikal). Their location and amplitude are therefore constrained by gravity signal only (Figure 11).

[24] Layers 5 and 6 ( $\sim 110$  and  $170 \text{ km}$  respectively) are characterized by a low density ( $-100 \text{ kg m}^{-3}$ ), low velocity ( $-3\%$ ) pattern in the central part of the region, beneath Lake Baikal. This body is sharply bounded by higher density ( $+150 \text{ kg m}^{-3}$ ) and velocity ( $+3.5\%$ ) zones to the NW and SE.

## 5.2. Testing the Sediment Correction

[25] We proceeded with a number of inversions in order to figure out the best initial model and to estimate the influence of sediments. It was first found that the correction of the gravity signal for the sediment effects does play a significant role in the results for the three upper layers. Differences ranging between  $-1100$  and  $+700 \text{ kg m}^{-3}$  were observed between the corrected and noncorrected final density models. For the velocity models, the variation was in the range  $-4.6\%$  to  $+9.9\%$ . A  $\pm 10\%$  change in the density contrast used for the sediment correction resulted in maximum change of  $\pm 5.6 \text{ mGal}$  in the gravity signal, and implied a maximum difference of  $\pm 50 \text{ kg m}^{-3}$  in the density contrast after inversion. As the standard deviation for the calculated parameter was  $100 \text{ kg m}^{-3}$  after inversion, we concluded that the error induced by uncertainty of the sediment correction was included in the final error term.

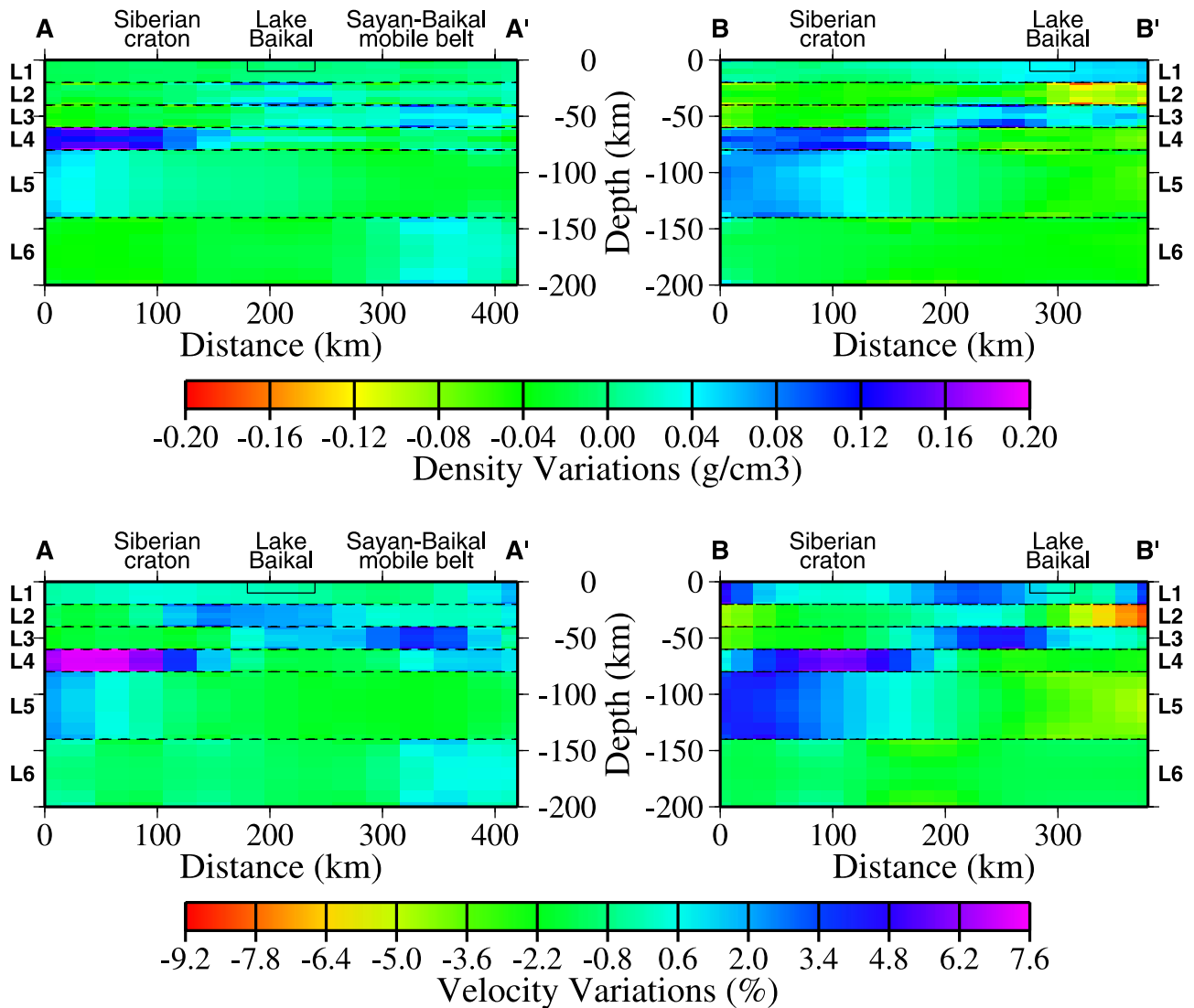


**Figure 6.** Two cross sections (AA' and BB') through the density and velocity models obtained after inversion. The  $L_n$  inscriptions and the dashed lines refer to the layer number and its depth limits. For the position of profiles, see layer 1 in Figure 5.

Besides, the effect on the velocity model was rather small, as a maximum difference of 1.0% was observed.

[26] The possible over- or underestimation of sediment correction was tested in a synthetic test. We artificially introduced a negative density and velocity perturbation in the first layer, simulating an undercorrection of the sediment (some sediment effects are still present). The initial perturbation was  $-300 \text{ kg m}^{-3}$  for the density and  $-15\%$  for the velocity perturbation. We proceed to a forward calculation of delay times and gravity signal, and the resulting synthetic data set was inverted by our joint inversion program, with the same input parameters as previously mentioned in this section. The results in density and velocity variations are shown in Figure 13 and discussed in the annex part. The maximum density and velocity contrasts are well retrieved in the upper layer, with a value of  $-10.8\%$  for velocity perturbation and  $-300 \text{ kg m}^{-3}$  for the density. The horizontal boundaries of the perturbing body are very well delimited, whereas small vertical checkboard effect can be

observed in the layer immediately under the upper one for the velocity model. However, this artifact is small ( $+3.6\%$ ) and limited within the crust. This means that even if the teleseismic ray crossing is not optimal for the upper layer, the addition of gravity signal allows to image crustal anomaly within the 20 first kilometers. If ever an under

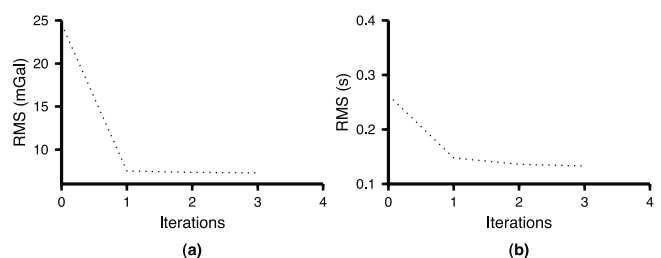


**Figure 7.** Variation of the root mean square (rms) for the gravity (a) and delay times (b) versus iteration number.

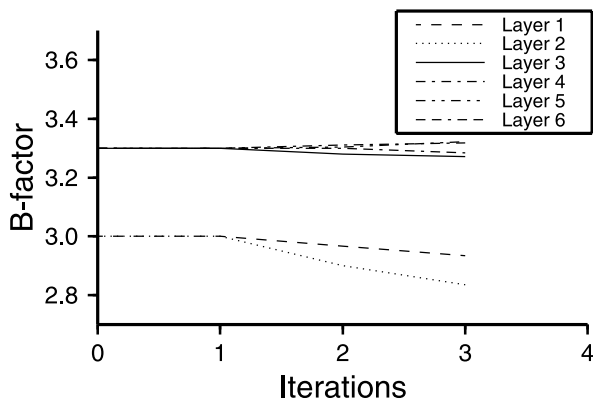


**Figure 8.** Evolution of the linear  $B$ -factor relating velocity and density ( $\Delta V_p = \mathbf{B}\Delta\rho$ ) through the iterations for the six layers of the models.

(or over-) estimation has been made in the correction of the sediment, we will then be able to locate it under Lake Baikal in the upper part of the model, and not misinterpret it as a real geodynamic items.

### 5.3. Testing the Smoothing Effect

[27] Another test was also carried out to evaluate the effect of smoothing constraint. As expected, the RMS decrease is bigger for low smoothing constraint. Mainly, the shape and wavelength of the density and velocity resulting perturbations do not change even with a drastic increase or decrease of the smoothing value. Only the amplitude of the perturbations is modified. For a smoothing 10 times smaller than the reference one, the density varies between  $-1200$  and  $+1000 \text{ kg m}^{-3}$  whereas the velocity is comprised between  $-15.3\%$  and  $+17.3\%$ . Conversely, with a smoothing 10 times larger, the density remains in the range  $-100 + 80 \text{ kg m}^{-3}$  and the velocity between  $-6.3\%$  and  $+4.9\%$ . These two end-members are far away from realistic value of contrast in the crust and the mantle, and we choose a smoothing parameter of 0.1 which allows for more realistic density and velocity contrasts.

### 5.4. Testing the $B$ -Factor

[28] The addition of the  $B$ -factor as a parameter in the inversion makes it less stable. When letting  $B$  vary more

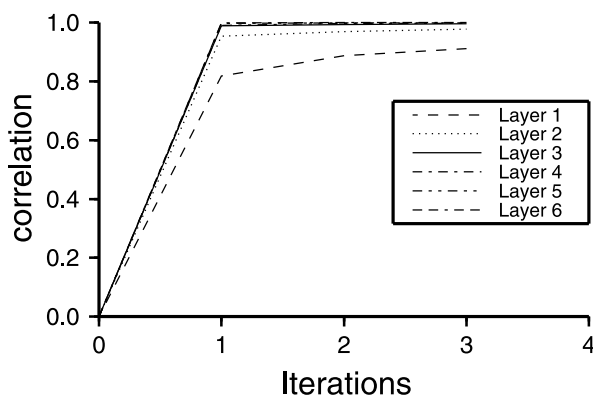


**Figure 9.** Evolution of the correlation between density and velocity contrasts through the iterations for each layer of the model.

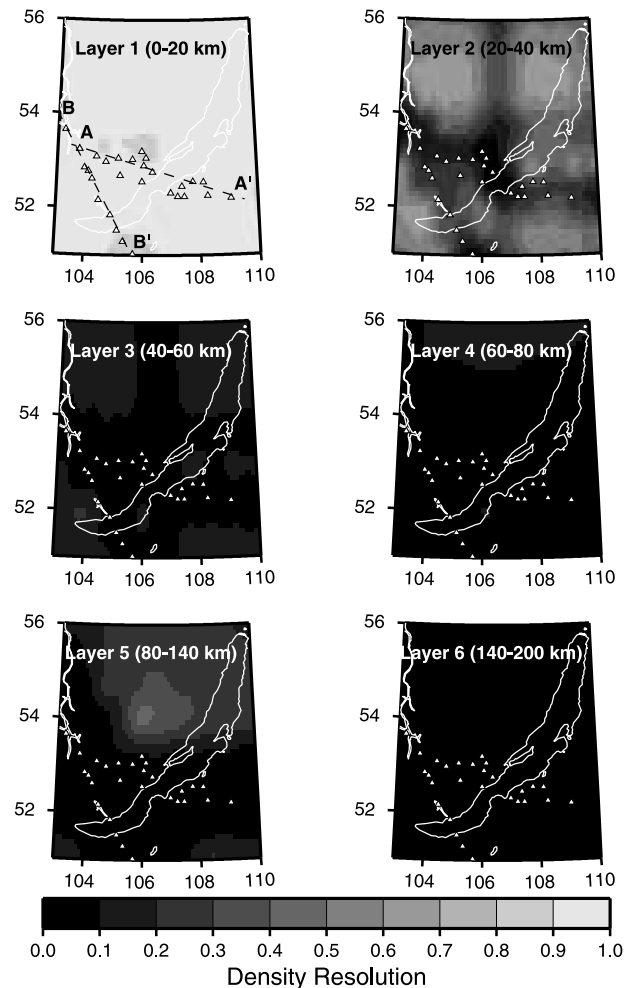


**Figure 10.** Resolution representation for each layer of the density model. The darker, the less resolved, the lighter, the best resolved. Telesismic stations are represented in white triangles.

freely (high standard deviation), the inversion hardly converges and unrealistic value for the parameters can appear (density contrast greater than  $4000 \text{ kg m}^{-3}$ ...). Even if this method allows to invert for  $B$ -factor, this parameter has to be in some way constrained to allow a good convergence of the results. The observed linearity between delay times and gravity anomalies plainly justifies the use of a  $B$ -factor not varying too much both with depth and laterally. We have tested several values of  $B$ . For higher ones ( $5$  and  $50 \text{ km s}^{-1} \text{ g}^{-1} \text{ cm}^3$ ), the RMS decrease is less than for  $B = 3 \text{ km s}^{-1} \text{ g}^{-1} \text{ cm}^3$ , indicative of a less suitable solution. For lower values ( $1$  and  $2 \text{ km s}^{-1} \text{ g}^{-1} \text{ cm}^3$ ), although the RMS decrease is a little better, the correlation coefficients between velocity and density contrasts for layers 1 and 2 are low. Thus, we chose a value for  $B$  ( $B = 3 \text{ km s}^{-1} \text{ g}^{-1} \text{ cm}^3$ ) that gives at the same time enough RMS decrease and good coefficients of correlation. Even if the determination of this parameter can not be perfectly defined and requires a subjective control of the initial value, the trend observed in the  $B$ -factor through iterations is however an additional information. As a matter of fact, the decrease of  $B$  in the two first layers ( $0$ – $40$  km) is in good agreement with studies for crustal and sediment rocks [e.g., Nafe and

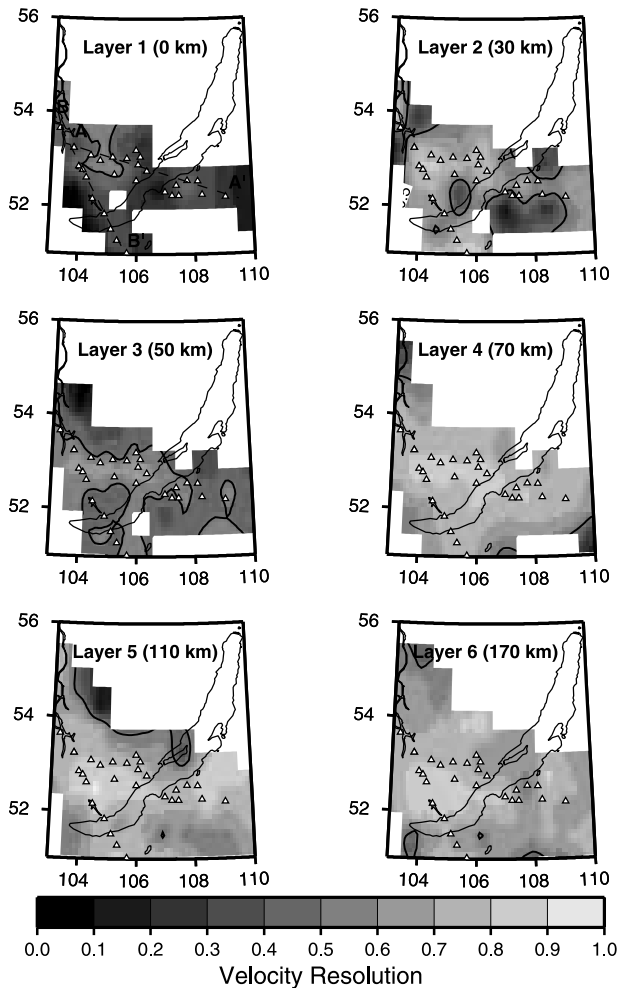


**Figure 11.** Resolution for velocity model. Heavy black line represents the 0.5 resolution limit, and white triangles are the seismic stations.

Drake, 1957; Christensen and Mooney, 1995] that proposed lower  $B$ -value for these types of rocks. This method is a way to allow for some variations in the choice of this  $B$ -factor, particularly with depth, which was not taken into account in the previous cooperative inversions. However, it asks for strong a priori constraint, and we propose to further investigate more suitable inversion schemes, such as Monte-Carlo or gradient ones to overcome this uncertainty.

## 6. Discussion

[29] We subdivide the following discussion part into two sections: the first one deals with the crustal interpretation of the models, the second one concerns the mantle part of the models. We insist on the fact that one has to jointly compare the density and velocity models to understand the geodynamical meaning of this joint inversion.

### 6.1. Upper and Lower Crustal Features

[30] The upper and lower crusts are represented by the two first layers in Figures 5 and 6, and correspond to the upper 40 kilometers.

[31] The velocity of the Siberian upper crust appears +2% faster than in the eastern part of the region (layer 1 in Figure

5), reflecting the structural difference between the Archean craton and the Paleozoic Sayan-Baikal belt. No sediment effect is observed in this layer under Lake Baikal, ruling out a possible over- or underestimation of the gravity field correction for sediments (see annex for synthetic test).

[32] The lower part of the crust (layer 2 in Figure 5) is dominated by high density and high velocity contrasts, that are horizontally inhomogeneous. This image is far from a single crustal thinning right beneath the topographic low of the rift one can associate in such a case. Instead, 3 dimensional patterns seem to control the crust-mantle boundary. Two of these features are located between the seismic profiles, on both sides of Lake Baikal. The southernmost feature corresponds to the Selenga topographic depression (SD in Figure 1) and is more likely to express a thinner crust. Since the northern one is clearly limited to the rift shoulder, it is likely related to the Moho depth variation beneath the rift flank. Both upward Moho flexure [van der Beek, 1997] and lower crust ductile flow [Petit *et al.*, 1997; Burov and Poliakov, 2001] are likely to compensate flank uplift (Figure 14). In case of flexural uplift, the Moho is shallower and the resulting density and velocity anomaly is thus positive. On the contrary, lower ductile flow is associated to crustal thickening, expressed by lower density and velocity. Hence, our model favors an upward flexure of the Moho as a mechanism to explain rift flank uplift at this place. Whether this thinning is related to inherited Mesozoic fabric [Delvaux *et al.*, 1995; Zorin, 1999] or Cenozoic extension [Delvaux *et al.*, 1997] cannot be resolved here.

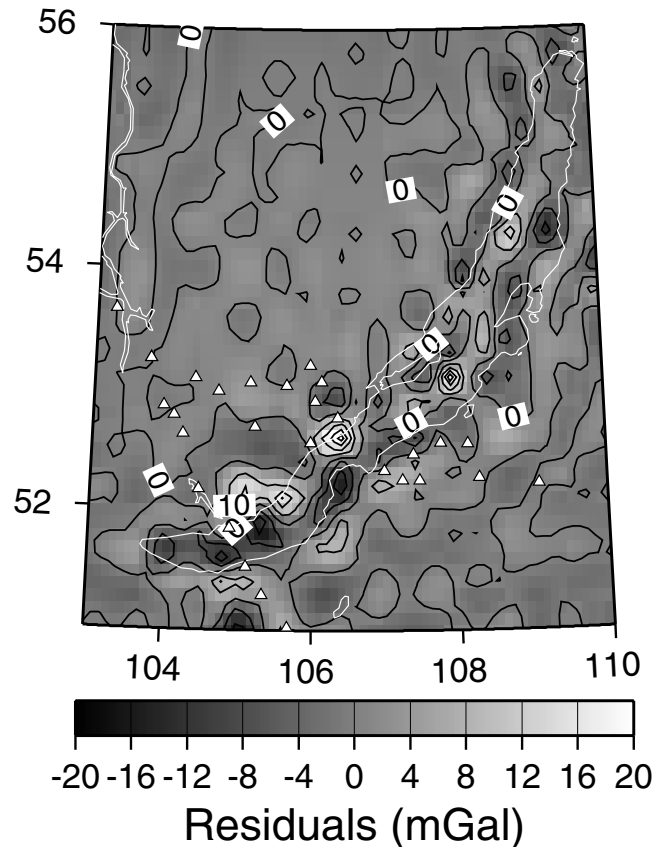


**Figure 12.** Initial minus calculated gravity anomaly residuals (mGal).

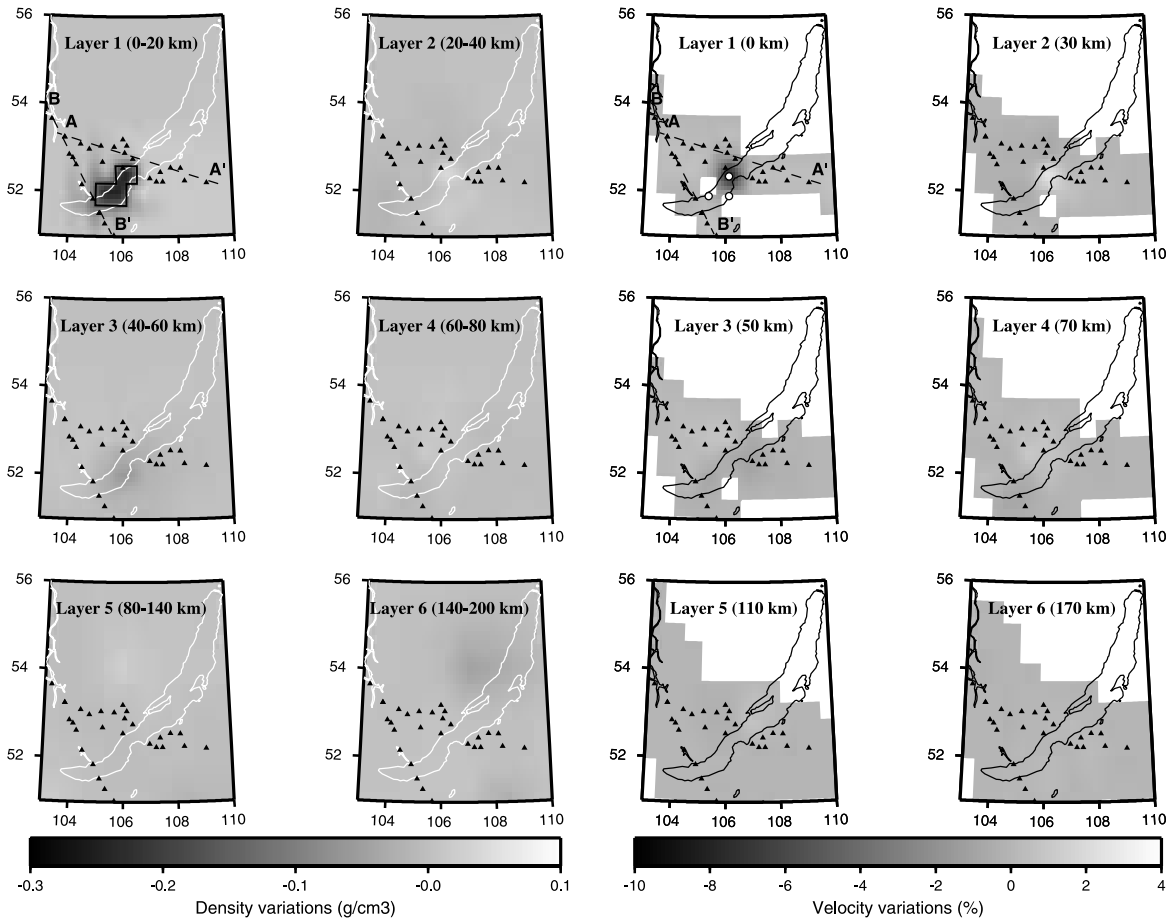


**Figure 13.** Density (left) and velocity (right) models of the different layers obtained in result of the joint inversion for synthetic sedimentary perturbation in the upper layer (0–20 km). The density blocks initially perturbed are shown by heavy lines in layer 1, and the perturbing velocity nodes are indicated on the velocity model by thick white points.

[33] Similarly, we relate the dense body located at the extreme western end of Lake Baikal in layer 2 (20–40 km) to the undercompensated area following the Sayan fault zone (SF in Figure 1) within the cratonic edge [Petit et al., 1997, 2002]. It can correspond to a local flexural effect of the fault, leading to a locally shallower Moho [Petit et al., 1997, profiles A and B on their Figure 15]. However, this pattern is only defined by gravity, and its nature has to be specified by further work. We image a low velocity-low density body just beneath the southern part of the seismic network near the edge of our area (Figure 5, layer 2). Achauer and Masson [2002] propose that this anomaly reflects the sediments in the lake. We prefer to relate it to the downward Moho deflection along the South Baikal Fault (Figure 1), first because this pattern is located south of the lake and second because the seismic rays hardly crossed within the upper 10 kilometers (anomaly could thus hardly be evidenced by tomography alone).

[34] A strong positive density contrast is located in the central part of Lake Baikal (Figure 5, layer 2), between central and northern basins (CBB and NBB in Figure 1, respectively). This anomaly even spreads through layers 3 and 4 with great amplitude (more than  $+300 \text{ kg m}^{-3}$ ). It explains the relative gravity high observed in the central part of the lake found after corrections for the sediment

effect. This area is not inverted in velocity model, as no ray pass through, and this anomaly is thus only constrained by gravity data. As ruled out by synthetic test (annex, Figure 16), the anomaly is likely to be overrated and

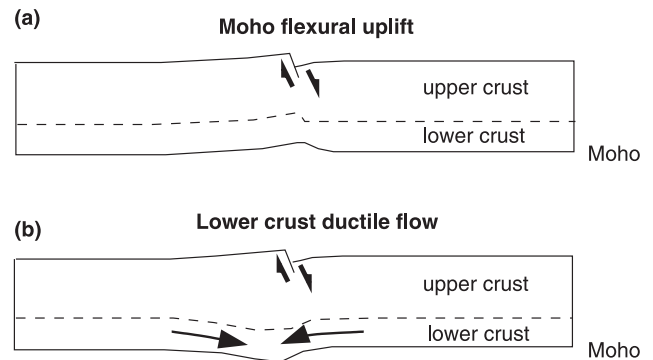


**Figure 14.** Two mechanisms likely to balance rift shoulder uplift. (a) In case of upward Moho flexure [from van der Beek, 1997], the depression caused by collapse of the hanging wall is compensated by a local upwarp of mantle material. (b) In case of lower crust flow, the flank uplift is maintained by crustal thickening [e.g., Burov and Poliakov, 2001].

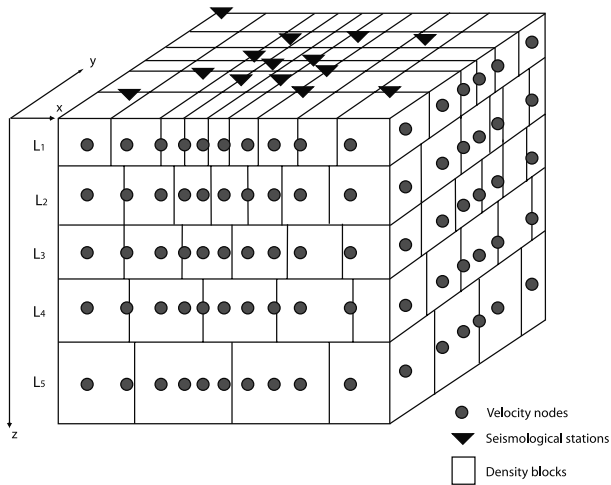


**Figure 15.** Schematic example for the model parameterization. Each layer ( $L_n$ ) is subdivided into density blocks and velocity nodes. The concentration of nodes and blocks can vary considering the stations location or data coverage, for example.

misplaced in this case. It is thus difficult to truthfully interpret this pattern from density model only. Nevertheless, it is worth noting that this anomaly is close to the oldest basin in Lake Baikal and at the junction of the lake to the Barguzin rift valley (Figure 1), a major rift bifurcation [Lesne *et al.*, 2000, and references therein]. Furthermore, its location corresponds to a potential crustal thinning, according to Petit *et al.* [1997]. Whether or not it can be related to Moho upwarping could only be investigated by further seismic field experiments and calls for more detailed data on thickness and density of sediments.

## 6.2. Mantle Anomalies

### 6.2.1. Short Wavelength Anomaly

[35] Structure of the upper mantle layer (layer 3, Figure 5) shows some patterns that are continuous downward from layer 2.

[36] At the eastern end of AA' seismic profile, a dense and fast body is well imaged by both seismic and gravity (layer 3, Figure 5). We have tested different thicknesses and depth boundaries for layer 3 in order to better localize the depth of this pattern. It appears that this anomaly only extends between 40 and 50 km depth. As it only concerns the uppermost part of the mantle, we may assume that it reflects a change in the Moho depth. We have to note here

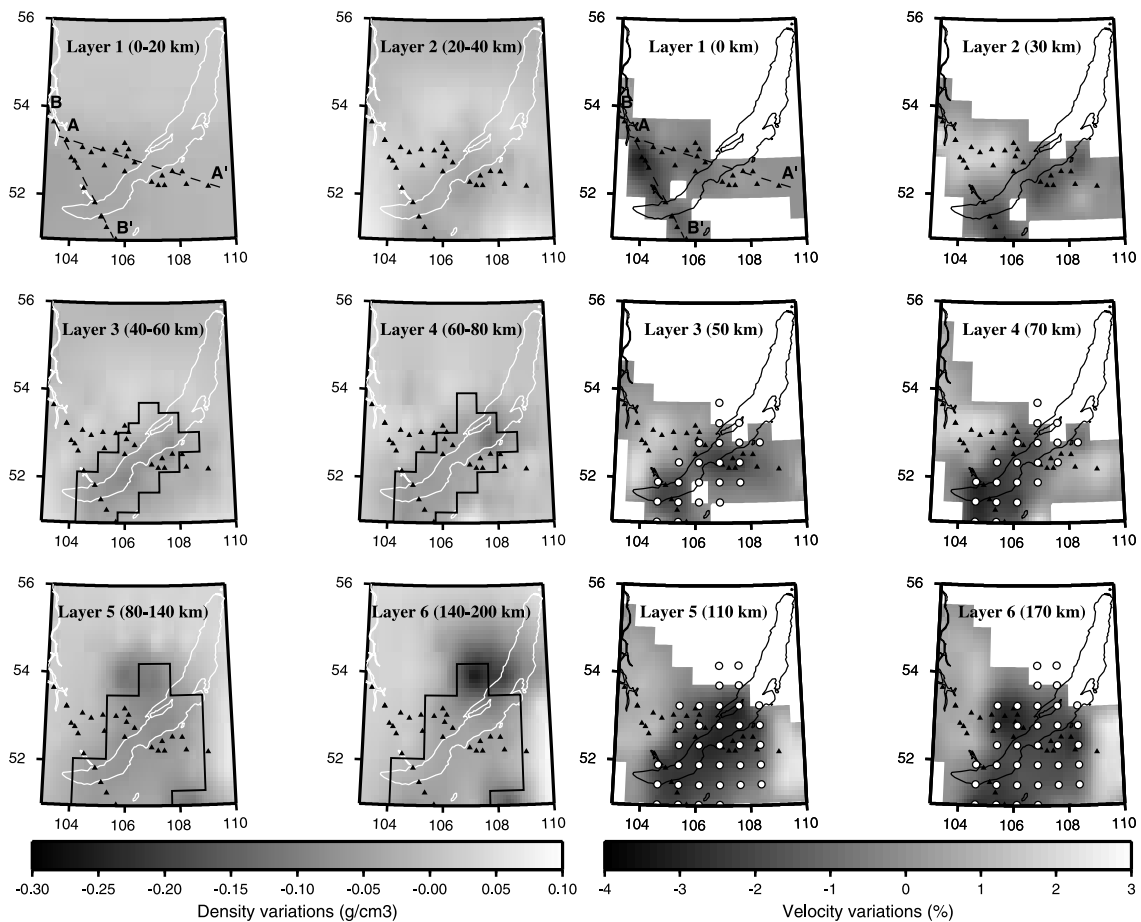


**Figure 16.** Density (left) and velocity (right) models of the different layers obtained in result of the joint inversion for synthetic asthenosphere up to 40 km depth. The perturbing density blocks and velocity nodes are represented by heavy lines and white points, respectively.

that the associated topography shows several basin and range structures parallel to the rift (Figure 1), suggesting a recent deformation distributed over  $\sim 300$  km at very slow strain rates [Lesne *et al.*, 2000].

[37] Finally, a strong negative localized anomaly appears at the SW end of the lake, from 40 to 80 km depth. As this anomaly is deduced from gravity only, its depth and thus its amplitude are hardly constrained (see annex, test 2). It is therefore difficult to discern whether it is a small crustal anomaly or a higher mantle one. However, it is worth noting that it is located where heat flow shows a local maximum [Lysack, 1992; Petit *et al.*, 1998].

### 6.2.2. Long Wavelength Anomaly

[38] The deeper mantle part of our models (i.e., layers 4 to 6, Figure 5) is characterized by a faster and denser Siberian craton mantle (north of Lake Baikal, Figure 1). An anomalously cold cratonic lithosphere is consistent with previous studies on cratonic areas which can be retrieved down to 250–300 km depth in some cases [e.g., Ritsema *et al.*, 1998; Forte and Perry, 2000]. A recent study by Artemieva and Mooney [2001] reaches the same conclusion, with a strong thermal contrast between the cold Archean Siberian Craton and the younger hotter lithospheric structures south of Lake Baikal. They show a NW-dipping cratonic lithosphere from the northern edge of Lake Baikal, which is consistent with our models (Figure 5, layers 4 and 5). A colder cratonic lithosphere is also in good agreement with the recent S-wave tomography of Villaseñor *et al.* [2001]. Even if their study presents less detailed resolution than ours, cross sections through Baikal rift zone show a fast cratonic mantle down to 200 km depth (C. Froidevaux, personal communication).

[39] The question of cratonic lithosphere stability via combination of negative thermal buoyancy and positive chemical buoyancy still remains debated [e.g., Jordan, 1978; Doin *et al.*, 1997; Forte and Perry, 2000]. The cratonic shields present a S-wave velocity/density relationship that differs from the normal lithosphere [Forte and Perry, 2000], and to stay stable the cratonic roots have to be buoyant (isostatically and/or dynamically) supported and more viscous than normal lithosphere [Doin *et al.*, 1997]. In our models the Siberian cratonic lithosphere appears denser and faster relative to adjacent asthenosphere beneath the rift axis where lithosphere is thinner. Thus, it still can be depleted and has lower density than normal lithosphere. Therefore, our results cannot discriminate between the proposed models for the craton formation and composition. We thus propose here that the higher values of density and velocity retrieved beneath the Siberian craton is more likely to reflect the contrast between this Archean structure and the asthenospheric material beneath the rift axis. As the cratonic shield seems to become thinner as we move from NW toward the rift axis, it may reflect thermal erosion of the craton by the mobile belt activation about 100–80 Ma ago [Jahn *et al.*, 2000].

[40] These results are somehow different from the previous study made by Petit *et al.* [1998], who found a low velocity anomaly at about 100 km depth beneath the Siberian craton. The lower resolution and a difference in the reference velocity probably explain this discrepancy. We argue here that a better ray sampling of the target volume (Figure 11) warrants a better location of anomaly

boundaries. Actually, a recent reconsideration of their teleseismic models [Bushenkova and Koulakov, 2001] leads to a better consistency between our results and their regional study.

[41] From about 70 km down to 170 km depth (layers 4 to 6, Figure 5) we find a low velocity ( $-3\%$ ), low density ( $-100 \text{ kg m}^{-3}$ ) body beneath the rift axis. It seems to widen with depth, and reaches  $-5\%$  velocity variation value. We have tested different layer depths, and 70 km is the shallowest depth where this anomaly first appears. Because of its wavelength, amplitude, shape and location, we interpret this pattern as the lithosphere-asthenosphere boundary combined with the thermal contrast coming from the cratonic mantle. We cannot fairly discriminate between these two effects, anyway we locate the lithosphere-asthenosphere boundary at a depth of about 70 km, and not at crustal depth as previously proposed by Gao *et al.* [1994]. We performed a test to be sure that an asthenospheric upwelling located above 70 km depth could not be retrieved by our inversion in deeper part of our model. In this test, reported in the annex (Figure 16), we introduced a perturbing body of  $-100 \text{ kg m}^{-3}$  for its density contrast and  $-3.7\%$  for its velocity from 50 km depth down to 170 km. The resulting models show a negative density and velocity contrast from 30 km depth instead of the initial 50 km (Figure 16). This is due to the smearing effect along the seismic rays that the density cannot totally overcome. This particularly well enlightens the fact that in Rift Baikal case the asthenosphere-lithosphere boundary on no account can be located at less than 70 km depth, and because of smearing effects still present and hardly quantified, we can even assume that this boundary is located deeper than 70 km. We explain the discrepancy between our study and the one from Gao *et al.* [1994] by both the addition of gravity data, and the use of fewer a priori assumptions. We only use here constant variance values, whereas Gao *et al.* [1994] already assumed that the main part of the delay times comes from an asthenospheric upwelling with a  $-5\%$  velocity contrast. As shown in this study, the thermal contrast between the cratonic shield and the surrounding areas can contribute to a large part of the signal in the upper mantle.

### 6.3. Extension, Sedimentation, and Heat Flow

[42] Let us now compare heat flow data in the Baikal rift zone with the structure obtained in our joint inversion. Heat flow in the Baikal area is very spatially variable. Two patterns can be observed by averaging the heat flow data on a 5 km interval grid. The regional trend of heat flow in the Baikal zone shows an increase from 30–45  $\text{mW m}^{-2}$  at the Siberian craton to 55–65  $\text{mW m}^{-2}$  in the Sayan-Baikal belt without considerable variations within the rift zone [Lysack, 1992; Lesne *et al.*, 2000]. Locally, one can observe sharp increase of the heat flow value, in some places up to 150–500  $\text{mW m}^{-2}$ . This local component correlates with position of faults, and Poort and Polyansky [2001] attributed it to groundwater flow driven by compaction and topography. Distribution of the regional heat flow is the result of the interaction of two main processes: an intraplate or mantle-induced extension which increases the heat flow, and a rather fast sedimentation process (about 1  $\text{km My}^{-1}$ ) which decreases its value. To estimate the influence of both

factors, we use a thermomechanical model of rheologically stratified Earth's outer shell, including the sedimentary layer, the crust, lithosphere and asthenosphere [Mikhailov *et al.*, 1996]. This model considers evolution of velocity and temperature fields in result of the deformation by external intraplate or mantle-induced forces, taking into account sedimentation and erosion. First, we consider an intraplate extension. Initial thickness of the crust and the lithosphere corresponded to the Sayan-Baikal zone and were set equal to 45 km and 100 km, respectively [Logatchev and Zorin, 1992]. Parameters of the extension were chosen so that during 5 My we form a rift zone 50 km wide and 6 km deep containing 5 km of sediments. As a result, the thickness of the crust below the rift zone was 33 km after 5 My extension, which corresponds rather well to observations in the central rift [Logatchev and Zorin, 1992]. The asthenosphere below the rift rose up to 70 km depth, which also coincides with the results of our joint inversion. For temperature calculation, the thermal diffusivity for crustal and lithospheric layers was equally assigned to  $10^{-6} \text{ m}^2 \text{ s}^{-1}$ . This parameter was taken five time bigger for the asthenosphere, accounting for possible heat transfer by basalt melt and convection. The heat generation within the sediments, crust and lithospheric mantle was equal to 0.1, 1.0 and  $0.05 \mu\text{W m}^{-3}$ , respectively. Calculated heat flow at the surface of the model shows a 20% decrease at the rift basin, and small increase up to 10–15% at its borders. These results were obtained not taking into account heat transfer by groundwater flow, in particular its topography-driven component. This process increases the regional heat flow in the lake, also causing considerable local variations. Combining results of our thermal modeling with estimates of Poort and Polyansky [2001], one can conclude that effects of extension and sedimentation compensate each other and that the model of intraplate extension predicting the top of the asthenosphere at 70 km depth fits well the regional features of the heat flow distribution. The models with larger extension and mantle-induced (active) rifting yield considerably higher heat flow. Indeed, enlarging intraplate extension ratio in order to drive the asthenosphere up to 40–45 km depth [Gao *et al.*, 1994] yields a Moho depth equal to 21 km and regional heat flow increase of more than 30% (assuming the same sedimentation rate and no groundwater circulation). These values do not fit existing data. For mantle-induced extension, the temperature of the mantle below the rift zone is assumed to be heightened, so that the regional heat flow anomaly should be much higher. Thus, the suggestion of a shallow asthenosphere depth does not agree with the regional heat flow observed in the Baikal rift zone.

## 7. Conclusions

[43] By jointly inverting gravity and teleseismic data, we are able to provide consistent density and velocity models that explain both data sets equally well in the southern Baikal rift. This method allows to reconcile two types of data that previously lead to contrasting interpretations [e.g., Gao *et al.*, 1994; Petit *et al.*, 1998]. It is thus a very useful tool to image the lithosphere, all the more because of the forthcoming gravity satellite data that will provide global coverage.

[44] The contrast between the Archean Siberian and the Paleozoic Sayan-Baikal orogenic lithosphere is clearly shown in our models. The upper crust as well as the upper

mantle part of the Archean Siberian craton appear faster and denser than the surroundings. The upper crust contrast can be explained by compositional differences between the Archean crust and the orogenic belt. The mantle contrasts, in good agreement with recent seismological studies, results from the combination of different processes. First, the cold and thick Archean craton lithosphere thermally contrasts with the hotter and thinner lithosphere of the Sayan-Baikal fold-and-thrust belt deformed during Mesozoic. Second, the uplift of lithosphere-asthenosphere boundary beneath the rift axis produces a low-density low-velocity feature that superimposes on the previous signal. Even if the cratonic mantle is chemically depleted, it thus produces a high density anomaly beneath the Archean region relative to the hot asthenospheric material. It is worth noting here that the lithosphere-asthenosphere boundary appears below 70 km depth in our models, contradicting the proposition from Zorin [1981] and Gao *et al.* [1994] who reduce the lithosphere to the crustal thickness beneath the rift axis ( $\sim 40$  km). Our models are also consistent with the regional heat flow when taking into account the sediments infilling in the lake. The extent of this low velocity, low density body below 200 km depth is questionable, as recent studies do not detect any velocity perturbation below 150–200 km [Priestley and Debayle, 2001; Achauer and Masson, 2002].

[45] Superimposed on this long wavelength anomalies, it was imaged short wavelength variations of the crust-mantle boundary, with a possible localized mantle upwarping in the central part of Lake Baikal. This geometry is far from the symmetric structure one can assume for a rifting process, and it evidences how atypical the Baikal rift could be. This complex 3-D Moho geometry and mantle anomalies can be related to mantle flow following the cratonic edges and impinging the crust in some sparse localized places. Thus, our results favor the idea that a deep-seated anomalous asthenosphere can slightly weaken the overriding lithosphere at a place characterized by inherited lateral heterogeneities [e.g., Ruppel, 1995; Petit *et al.*, 1998].

[46] The different driving forces such as India-Eurasia collision, Pacific subduction, basal drag, and the role of thermal and mechanical mechanisms could only be deduced from further thermomechanical modeling. This study can then be used as an a priori information for these kinds of models, and leads to better constrain lithospheric structure and structure evolution for the Baikal rift.

## Appendix A: Synthetic Tests

### A1. Sediment Underestimation

[47] A negative density ( $\Delta\rho = -300 \text{ kg m}^{-3}$ ) and velocity perturbation (15%) has been introduced in the upper layer (0–20 km) just beneath Lake Baikal to simulate an underestimation of the sediment effect. After jointly inverted the synthetic data with homogeneous density and velocity starting models, the results are shown in Figure 13. The initial standard errors on density and velocity were homogeneously set to  $\pm 300 \text{ kg m}^{-3}$  and  $\pm 0.3 \text{ km s}^{-1}$ , respectively. The perturbation is better retrieved in density than in velocity output model, both in location and in amplitude. The retrieved density anomaly is  $-330 \text{ kg m}^{-3}$  and for the velocity perturbation the maximum is  $-10.8\%$ . Because of the poor ray density near the surface, two initially perturbed

nodes are not inverted and the method is only able to locate the perturbation in one velocity node. Moreover, an artifact is present in layer 2 in the velocity model, where a smearing effect of inverse polarity (that we call “checkbox effect”) obviously spreads downward. The amplitude of this effect is smaller in density, and we are then able to detect its nature thanks to the combination of the two kinds of data.

[48] Even if the ray crossing is certainly poor in the 10 first kilometers, an under- or overestimation in the sediment correction will be imaged by the joint inversion. It is worth noting here also that a negative velocity perturbation is much more difficult to be imaged than a positive one, because the rays tend to pass round rather than through it. Its amplitude is then hardly completely recovered, and in this case, the combination with gravity data helps to locate and identify the perturbing body.

## A2. Asthenospheric Effect

[49] To simulate the effect of an asthenosphere up to 40 km depth, we introduced a negative perturbation (due to heat) both in density and velocity models for the layers 3 to 6. The initial density perturbation was set to  $100 \text{ kg m}^{-3}$  and the velocity variation was equal to about 3.7% (computed from the density with a  $B$ -factor of  $3 \text{ km s}^{-1} \text{ g}^{-1} \text{ cm}^3$ ). The initial parameters and the parametrization were the same as those taken for the main joint inversion. By inversion of the synthetic data computed after this model, we obtain the resulting density and velocity models depicted in Figure 16. The perturbing body is quite well retrieved in both models (density and velocity), but at a shallower depth than initially input. It is already present in layer 2, at 30 km depth, with a maximum density contrast of  $-50 \text{ kg m}^{-3}$ , and a maximum velocity perturbation of  $-3\%$ . For layers 3 to 5, the density and velocity perturbations reach  $-100 \text{ kg m}^{-3}$  and  $-3\%$ , respectively. At greater depth, especially at 170 km, the perturbing body is better located in velocity than in density, except for the extreme northern density block, where a  $-300 \text{ kg m}^{-3}$  density contrast appears. This is coming from the fact that at this particular location the velocity nodes are not inverted, and the information concentrates into the density model in spite of the precautions we have taken. The inversion tries to explain the gravity signal existing in this area, and puts some excessive density in the last layer. This effect can hardly be avoided without any specific a priori assumption. However, in the zone of initial perturbation (delimited by black lines in Figure 16), the resulting density contrast ( $-80 \text{ kg m}^{-3}$ ) is fairly close to the initial one ( $-100 \text{ kg m}^{-3}$ ).

[50] **Acknowledgments.** We would like to thank M. Jordan for stimulating discussions about the joint inversion technique. Many thanks to C. Froidevaux for his fruitful discussion about the Pacific subduction role in the Baikal extension and his Baikal tomographic cross sections. We would like to thank C. Ebinger for her critical review. We are grateful to the anonymous Associate Editor and two reviewers for their thorough reviews. C. T. was funded by a Marie-Curie Fellowship (grant HPMFCT-2000-00630). This is IGP contribution 1857.

## References

Abers, G., Three-dimensional inversion of regional  $p$  and  $s$  arrival times in the East Aleutians and sources of subduction zone gravity highs, *J. Geophys. Res.*, *99*, 4395–4412, 1994.  
 Achauer, U., and F. Masson, Seismic tomography of continental rifts revisited: From relative to absolute heterogeneities, *Tectonophysics*, *358*, 17–37, 2002.

Artemieva, I., and W. Mooney, Thermal thickness and evolution of Precambrian lithosphere: A global study, *J. Geophys. Res.*, *106*, 16,387–16,414, 2001.  
 Birch, F., The velocity of compressional waves in rocks to 10 kilobars, 2, *J. Geophys. Res.*, *66*, 2199–2224, 1961.  
 Blakely, R., *Potential Theory in Gravity and Magnetic Applications*, Cambridge Univ. Press, p. 441, New York, 1995.  
 Burov, E., and A. Poliakov, Erosion and rheology controls on synrift and postrift evolution: Verifying old and new ideas using a fully coupled numerical model, *J. Geophys. Res.*, *106*, 16,461–16,481, 2001.  
 Burov, E., F. Houdry, M. Diament, and J. Déverchère, A broken plate beneath the North Baikal rift zone revealed by gravity modelling, *Geophys. Res. Lett.*, *21*, 129–132, 1994.  
 Bushenkova, N., and Y. Koulakov, Tomography on PP-P waves and its application for investigation of the upper mantle in central Siberia, *Geophys. Res. Abstr.*, vol. 3, p. 70, EGS XXVI General Assembly, 2001.  
 Calais, E., et al., Crustal deformation in the Baikal rift from GPS measurements, *Geophys. Res. Lett.*, *25*, 4003–4006, 1998.  
 Christensen, N. I., and W. D. Mooney, Seismic velocity structure and composition of the continental crust: A global view, *J. Geophys. Res.*, *100*, 9761–9788, 1995.  
 Delvaux, D., R. Moeys, G. Stapel, A. Melnikov, and V. Ermikov, Paleostress reconstructions and geodynamics of the Baikal region, Central Asia, 1, Paleozoic and Mesozoic pre-rift evolution, *Tectonophysics*, *252*, 61–101, 1995.  
 Delvaux, D., R. Moeys, G. Stapel, C. Petit, K. Levi, A. Miroshnichenko, V. Ruzhich, and V. San'kov, Paleostress reconstructions and geodynamics of the Baikal region, Central Asia, 2, Cenozoic rifting, *Tectonophysics*, *282*, 1–38, 1997.  
 Déverchère, J., F. Houdry, N. Solonenko, A. Solonenko, and V. Sankov, Seismicity, active faults and stress field of the North Muya region, Baikal rift: New insights on the rheology of extended continental lithosphere, *J. Geophys. Res.*, *98*, 19,895–19,912, 1993.  
 Déverchère, J., C. Petit, N. Gileva, N. Radziminovitch, V. Melnikova, and V. San'kov, Depth distribution of earthquakes in the Baikal rift system and its implications for the rheology of the lithosphere, *Geophys. J. Int.*, *146*, 714–730, 2001.  
 Diament, M., and M. Kogan, Longwavelength gravity anomalies and the deep thermal structure of the Baikal rift, *Geophys. Res. Lett.*, *17*, 1977–1980, 1990.  
 Doin, M.-P., L. Fleitout, and U. Christensen, Mantle convection and stability of depleted and undepleted continental lithosphere, *J. Geophys. Res.*, *102*, 2771–2787, 1997.  
 Forte, A., and C. Perry, Geodynamical evidence for a chemically depleted continental tectosphere, *Science*, *290*, 1940–1944, 2000.  
 Gao, S., M. Davis, H. Liu, P. Slack, Y. Zorin, N. Logatchev, M. Kogan, P. Burkholder, and R. Meyer, Asymmetric upward of the asthenosphere beneath the Baikal rift zone, Siberia, *J. Geophys. Res.*, *99*, 15,319–15,330, 1994.  
 Gao, S., P. Davis, H. Liu, P. Slack, A. Rigor, Y. Zorin, V. Mordvinova, V. Kozhevnikov, and N. Logatchev, SKS splitting beneath continental rift zones, *J. Geophys. Res.*, *102*, 22,781–22,797, 1997.  
 Garner, J., S. Gibson, R. Thompson, and G. Nowell, Contribution of pyroxenite-derived melts to Baikal rift-related magmatism, *Eos Trans. AGU*, *82*(47), Fall Meet. Suppl., F1396, 2001.  
 Huismans, R., Y. Podladchikov, and S. Cloetingh, Transition from passive to active rifting: Relative importance of asthenospheric doming and passive extension of the lithosphere, *J. Geophys. Res.*, *106*, 11,271–11,291, 2001.  
 Hutchinson, D., A. Golmshtok, L. Zonenshain, T. S. C. Moore, and K. Klitgord, Depositional and tectonic framework of the rift basins of Lake Baikal from multichannel seismic data, *Geology*, *20*, 589–592, 1992.  
 Ionov, D., Mantle structure and rifting process in the Baikal-Mongolia region: Geophysical data and evidence from xenoliths in volcanic rocks, *Tectonophysics*, *351*, 41–60, 2002.  
 Ionov, D., S. O'Really, and I. Ashchepkov, Feldspar-bearing lherzolite xenoliths in alkalibasalts from Hamar-Daban, southern Baikal region, Russia, *Contrib. Mineral. Petrol.*, *122*, 174–190, 1995.  
 Jahn, B., F. Wu, and B. Chen, Massive granitoid generation in Central Asia: Nd isotope evidence and implication for continental growth Phanerozoic, *Episodes*, *23*, 82–92, 2000.  
 Jordan, M., and U. Achauer, A new method for the 3-d joint inversion of teleseismic delaytimes and bouguer gravity data with application to the French Massif Central, *Eos Trans. AGU*, *80*(46), Fall Meet. Suppl., F696, 1999.  
 Jordan, T., Composition and development of the continental tectosphere, *Nature*, *274*, 544–548, 1978.  
 Koulakov, I., Three-dimensional seismic structure of the upper mantle beneath the central part of the Eurasian continent, *Geophys. J. Int.*, *133*, 467–489, 1998.

- Lees, J., and J. VanDecar, Seismic tomography constrained by Bouguer gravity anomalies: Applications in Western Washington, *Pure Appl. Geophys.*, *135*, 31–52, 1991.
- Lesne, O., E. Calais, J. Déverchère, J. Chéry, and R. Hassani, Dynamics of intracontinental extension in the North Baikal rift from two-dimensional numerical deformation modeling, *J. Geophys. Res.*, *105*, 21,727–21,744, 2000.
- Li, X., and M. Chouteau, Three-dimensional gravity modeling in all space, *Surv. Geophys.*, *19*, 339–368, 1998.
- Lines, L., A. Schultz, and S. Treitel, Cooperative inversion of geophysical data, *Geophysics*, *53*, 8–20, 1988.
- Logatchev, N., and Y. Zorin, Evidence and causes of the two-stage development of the Baikal Rift, *Tectonophysics*, *143*, 225–234, 1987.
- Logatchev, N., and Y. Zorin, Baikal rift zone: Structure and geodynamics, *Tectonophysics*, *208*, 273–286, 1992.
- Logatchev, N., Y. Zorin, and V. Rogozhina, Baikal rift: Active or passive? Comparison of the Baikal and Kenya rift zone, *Tectonophysics*, *94*, 223–240, 1983.
- Lysack, S., Heat flow variations in continental rifts, *Tectonophysics*, *208*, 309–323, 1992.
- Mikhailov, V., V. Myasnikov, and E. Timoshkina, Dynamics of the Earth's outer shell evolution under extension and compression, *Phys. Solid Earth*, *32*, 496–502, 1996.
- Molnar, P., and P. Tapponnier, Cenozoic tectonics of Asia/Effects of a continental collision, *Science*, *189*, 419–426, 1975.
- Nafe, J. E., and C. L. Drake, Variation with depth in shallow and deep water marine sediments of porosity, density, and the velocity of compressional and shear waves, *Geophysics*, *22*, 523–552, 1957.
- Nataf, H.-C., C. Froidevaux, J.-L. Levrat, and M. Rabinowicz, Laboratory convection experiments: The effect of lateral cooling and generation of instabilities in the horizontal layers, *J. Geophys. Res.*, *86*, 6143–6154, 1981.
- Nicolas, A., U. Achauer, and M. Daigner, Rift initiation by lithosphere rupture, *Earth Planet. Sci. Lett.*, *123*, 281–298, 1994.
- Petit, C., and J. Déverchère, Velocity structure of the northern Baikal rift, Siberia, from local and regional earthquake travel times, *Geophys. Res. Lett.*, *22*, 1677–1680, 1995.
- Petit, C., J. Déverchère, F. Houdry, V. Sankov, and V. Melnikova, Present-day stress field changes along the Baikal rift and tectonic implications, *Tectonics*, *15*, 1171–1191, 1996.
- Petit, C., E. Burov, and J. Déverchère, On the structure and mechanical behaviour of the extending lithosphere in the Baikal Rift from gravity modelling, *Earth Planet. Sci. Lett.*, *149*, 29–42, 1997.
- Petit, C., I. Koulakov, and J. Déverchère, Velocity structure around the Baikal rift zone from teleseismic and local earthquake travel times and geodynamic implications, *Tectonophysics*, *296*, 124–144, 1998.
- Petit, C., J. Déverchère, E. Calais, V. San'kov, and D. Fairhead, Deep structure and mechanical behavior of the lithosphere in the Hangai-Hövs-göl region, Mongolia: New constraints from gravity modeling, *Earth Planet. Sci. Lett.*, *197*, 133–149, 2002.
- Poort, J., and O. Polyansky, Heat transfer by groundwater flow during the Baikal rift evolution, *Tectonophysics*, *351*, 75–89, 2001.
- Priestley, K., and E. Debayle, Lithospheric structure of the Siberian shield from surface wave tomography, *Eos Trans. AGU*, *82(47)*, Fall Meet. Suppl., F813, 2001.
- Ritsema, J., S. Ni, D. Helmberger, and H. Crotwell, Evidence for strong shear velocity reductions and velocity gradients in the lower mantle beneath Africa, *Geophys. Res. Lett.*, *25*, 4245–4248, 1998.
- Ruppel, C., Extensional processes in continental lithosphere, *J. Geophys. Res.*, *100*, 24,187–24,215, 1995.
- Ruppel, C., M. Kogan, and M. McNutt, Implications of new gravity data for Baikal rift zone structure, *Geophys. Res. Lett.*, *20*, 1635–1638, 1993.
- Steck, L., and W. Prothero, A 3-D raytracer for teleseismic body-wave arrival times, *Bull. Seismol. Soc. Am.*, *81*, 1332–1339, 1991.
- ten Brink, U., and M. Taylor, Crustal structure of central Lake Baikal: Insights into intracontinental rifting, *J. Geophys. Res.*, *107(B7)*, 2132, doi:10.1029/2001JB000300, 2002.
- Thurber, C. H., Earthquake locations and three-dimensional crustal structure in the Coyote Lake Area, central California, *J. Geophys. Res.*, *88*, 8226–8236, 1983.
- Tiberi, C., M. Diament, H. Lyon-Caen, and T. King, Moho topography beneath the Corinth rift area (Greece) from inversion of gravity data, *Geophys. J. Int.*, *145*, 797–808, 2001.
- Tommasi, A., and A. Vauchez, Continental rifting parallel to ancient collisional belts: An effect of the mechanical anisotropy of the lithospheric mantle, *Earth Planet. Sci. Lett.*, *185*, 199–210, 2001.
- van der Beek, P., Flank uplift and topography at the central Baikal Rift (SE Siberia): A test of kinematic models for continental extension, *Tectonics*, *16*, 122–136, 1997.
- Vauchez, A., G. Barruol, and A. Tommasi, Why do continents break up parallel to ancient orogenic belts?, *Terra Nova*, *9*, 62–66, 1997.
- Vauchez, A., A. Tommasi, and G. Barruol, Rheological heterogeneity, mechanical anisotropy and deformation of the continental lithosphere, *Tectonophysics*, *296*, 61–86, 1998.
- Vernant, P., F. Masson, R. Bayer, and A. Paul, Sequential inversion of local earthquake traveltimes and gravity anomaly—The example of the Western Alps, *Geophys. J. Int.*, *150*, 79–90, 2002.
- Villaseñor, A., M. Ritzwoller, A. Levshin, M. Barmin, E. Engdahl, W. Spakman, and J. Trampert, Shear velocity structure of central Eurasia from inversion of surface wave velocities, *Phys. Earth Planet. Inter.*, *123*, 169–184, 2001.
- Zeyen, H., and U. Achauer, Joint inversion of teleseismic delay times and gravity anomaly data for regional structures: Theory and synthetic examples, in *Upper Mantle Heterogeneities From Active and Passive Seismology*, NATO Workshop, edited by K. Fuchs, pp. 155–168, Kluwer Acad., Norwell, Mass., 1997.
- Zorin, Y., The Baikal rift: An example of the intrusion of asthenospheric material into the lithosphere as the cause of disruption of the lithosphere plates, *Tectonophysics*, *73*, 91–104, 1981.
- Zorin, Y., Geodynamics of the western part of the Mongolia-Okhotsk collisional belt, Trans-Baikal region (Russia) and Mongolia, *Tectonophysics*, *306*, 33–56, 1999.
- Zorin, Y., V. Kozhevnikov, M. Novoselova, and E. Turutanov, Thickness of the lithosphere beneath the Baikal rift zone and adjacent regions, *Tectonophysics*, *168*, 327–337, 1989.
- U. Achauer, Manteau et Sismologie Large Bande, Ecole et Observatoire des Sciences de la Terre, Strasbourg, France.
- J. Déverchère, Institut Universitaire Européen de la Mer, Domaines Océaniques UMR 6538, Université de Bretagne Occidentale, Technopole Brest-Iroise, France.
- M. Diament, Laboratoire de Gravimétrie et Géodynamique, Département de Géophysique Spatiale et Planétaire UMR 7096, Institut de Physique du Globe, Paris, France.
- V. Mikhailov and S. Tikhotsky, Institute of Physics of the Earth RAS, Moscow, Russia.
- C. Petit-Mariani and C. Tiberi, Laboratoire de Tectonique UMR 7072, Université Paris 6, 4 Place Jussieu, T26-16 BP 129, 75252 Paris, Cedex 05, France.